

## Controlled dc Monitoring of a Superconducting Qubit

A. Kringhøj<sup>1</sup>, T. W. Larsen<sup>1</sup>, B. van Heck<sup>2,3</sup>, D. Sabonis<sup>1</sup>, O. Erlandsson<sup>1</sup>, I. Petkovic<sup>1</sup>, D. I. Pikulin<sup>2</sup>,  
P. Krogstrup<sup>1,4</sup>, K. D. Petersson<sup>1</sup>, and C. M. Marcus<sup>1</sup>

<sup>1</sup>Microsoft Quantum Lab Copenhagen and Center for Quantum Devices, Niels Bohr Institute, University of Copenhagen, Universitetsparken 5, 2100 Copenhagen, Denmark

<sup>2</sup>Microsoft Quantum, Station Q, University of California, Santa Barbara, California 93106-6105, USA

<sup>3</sup>Microsoft Quantum Lab Delft, Delft University of Technology, 2600 GA Delft, Netherlands

<sup>4</sup>Microsoft Quantum Materials Lab Copenhagen, Kanalvej 7, 2800 Lyngby, Denmark



(Received 17 October 2019; accepted 23 December 2019; published 5 February 2020)

Creating a transmon qubit using semiconductor-superconductor hybrid materials not only provides electrostatic control of the qubit frequency, it also allows parts of the circuit to be electrically connected and disconnected *in situ* by operating a semiconductor region of the device as a field-effect transistor. Here, we exploit this feature to compare in the same device characteristics of the qubit, such as frequency and relaxation time, with related transport properties such as critical supercurrent and normal-state resistance. Gradually opening the field-effect transistor to the monitoring circuit allows the influence of weak-to-strong dc monitoring of a “live” qubit to be measured. A model of this influence yields excellent agreement with experiment, demonstrating a relaxation rate mediated by a gate-controlled environmental coupling.

DOI: [10.1103/PhysRevLett.124.056801](https://doi.org/10.1103/PhysRevLett.124.056801)

Josephson junctions (JJs) serve as key elements in a wide range of quantum systems of interest for fundamental explorations and technological applications. JJs, which provide the nonlinearity essential for superconducting qubits [1], are typically fabricated using insulating tunnel junctions between superconducting metals [2]. Alternative realizations using atomic contacts [3] or superconductor-semiconductor-superconductor (S-Sm-S) junctions [4–6] are receiving growing attention. Hybrid S-Sm-S JJs host a rich spectrum of new phenomena, including a modified current-phase relation (CPR) [7,8] different from the sinusoidal CPR of metal-insulator-metal tunnel junctions. Other electrostatically tunable parameters include the sub-gap density of states (DOS), shunt resistance [9], spin-orbit coupling [10], and critical current [11].

Recent work on S-Sm-S JJs in various platforms relies on either dc (direct current) transport [8,12] or cQED (circuit quantum electrodynamics) qubit measurements [13–16]. Common to these experiments is that valuable device information is only accessible in one of the two measurement techniques. For instance, measurements estimating individual transmission eigenvalues [17] or measurements probing the local DOS are directly accessible with dc transport but not with cQED. The prospect of combining these techniques potentially allows a deeper understanding of JJ-based quantum systems.

In this Letter, we investigate a modified S-Sm-S JJ design of a gatemon qubit that combines dc transport and coherent cQED qubit measurements. The device is realized in an InAs nanowire with a fully surrounding epitaxial Al shell by removing the Al layer in a second region (besides

the JJ itself) allowing that region to function as a field-effect transistor (FET). By switching the FET between being conducting (“on”) or depleted (“off”) using a gate voltage, we are able to implement a controlled transition between the transport and cQED measurement configurations. We demonstrate that the additional tunability does not compromise the quality of the qubit in the cQED configuration, where the FET is off. We further demonstrate control of the qubit relaxation as the FET is turned on, continuously increasing the coupling of the junction to the environment, in agreement with a simple circuit model. Finally, we demonstrate strong correlation between cQED and transport data by comparing the measured qubit frequency spectrum with the switching current directly measured *in situ*.

Devices were fabricated on a high resistivity silicon substrate covered with a 20 nm NbTiN film. The nanowire region, qubit-capacitor island, electrostatic gates, on-chip gate filters, readout resonator, and transmission line were patterned by electron-beam lithography and defined by reactive-ion etching techniques; see Fig. 1(a). The full-shell InAs/Al epitaxial hybrid nanowire is placed at the bottom of the qubit island; see Fig. 1(b) [18]. Two gateable regions are formed by selective wet etching of the Al in two ~150 nm segments defined by electron-beam lithography, aligned with two independent bottom gates, which are separated from the nanowire by a 15-nm-thick HfO<sub>2</sub> dielectric. The three superconducting segments—ground, qubit island with capacitance  $C_Q$ , and dc bias  $V_J$ —are then contacted with ~200 nm sputtered NbTiN; see Fig. 1(b). In this circuit, when the FET is on, dc current or voltage

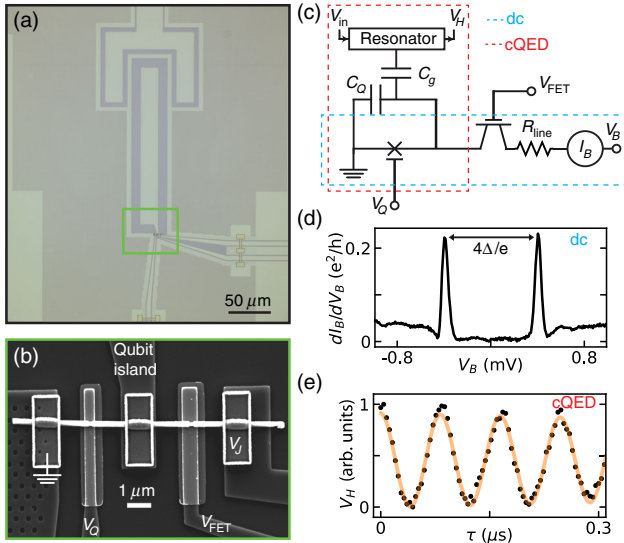


FIG. 1. (a) Optical micrograph of the modified gatemon qubit device showing the bottom of the readout resonator capacitively coupled to the qubit island. The island is contacted to a nanowire placed in the highlighted green square. (b) Scanning electron micrograph (SEM) of the nanowire in the green rectangle in (a). Two removed segments of the Al shell form the qubit JJ (125 nm) and the FET (175 nm), controlled by gates  $V_Q$  and  $V_{FET}$ . The bias voltage across the nanowire is indicated  $V_J$ . (c) Device circuit with FET off for cQED (dashed red box), and FET on allowing transport (dashed blue box). The bias voltage  $V_B$  refers to the total voltage drop across both the nanowire and line resistance  $R_{line}$ . (d) Differential conductance  $dI_B/dV_B$  as a function of bias voltage  $V_B$  shows the superconducting gap  $\Delta$  of the qubit JJ, with  $V_{FET} = +4$  V and  $V_Q = -2.9$  V. (e) Rabi oscillations of the qubit seen in resonator output  $V_H$  as a function of drive time  $\tau$  at  $V_{FET} = -3$  V and  $V_Q = -2.5$  V, with exponentially damped sinusoid (orange).

measurements are available [blue box in Fig. 1(c)]. Depleting the FET allows the device to operate as a qubit, where measurements of the heterodyne demodulated transmission  $V_H$  allow qubit state determination and  $V_Q$  allows tuning the qubit frequency  $f_{01}$  over several gigahertz [red box in Fig. 1(c)].

Setting the voltage on the FET gate to  $V_{FET} = +4$  V, which turned the FET fully conducting, and the voltage on the qubit JJ to  $V_Q = -2.9$  V makes the voltage drop predominantly across the qubit JJ. In this configuration, the differential conductance  $dI_B/dV_B$  probes the convolution of the DOS on each side of the JJ; see Fig. 1(d). Keeping in mind a simple model of JJ spectroscopy [9], we interpret the distance between the two peaks in  $dI_B/dV_B$  as  $4\Delta/e = 4 \times 190 \mu\text{V}$ , where  $\Delta$  is the induced superconducting gap. In the cQED configuration, with  $V_{FET} = -3$  V and  $V_Q = -2.5$  V, coherent Rabi oscillations are observed by varying the duration  $\tau$  of the qubit drive tone at the qubit frequency  $f_{01} = 4.6$  GHz. Following the drive tone, a second tone was applied at the readout resonator frequency,  $f_R \sim 5.3$  GHz, to perform dispersive readout where  $V_H$  is

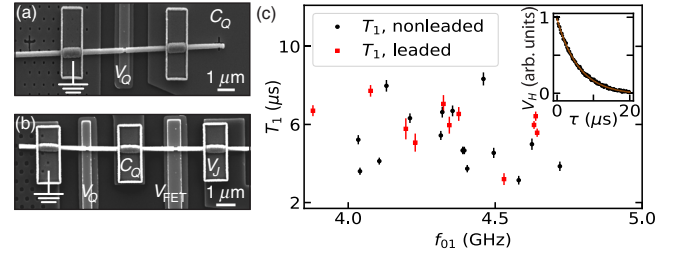


FIG. 2. (a) Scanning electron micrograph of a gatemon without transport lead.  $C_Q$  is the capacitance of the qubit island. (b) Same as (a) for gatemon with transport lead, with voltage bias  $V_J$ . (c) Qubit relaxation times  $T_1$  of the gatemons as a function of qubit frequency  $f_{01}$ . Both leaded (black circle) and nonleaded (red square) devices show similar  $T_1$  times between 3–8  $\mu\text{s}$ , with comparable mean and standard deviation values. Inset: Relaxation time  $T_1$  (black points) at  $f_{01} = 4.6$  GHz for the leaded device as a function of wait time  $\tau$ , with exponential fit (orange curve) yielding  $T_1 = 6 \mu\text{s}$ . Error bars are estimated from fit uncertainties.

measured; see Fig. 1(e). These experiments are carried out in a dilution refrigerator with a base temperature of  $\sim 10$  mK using standard lock-in and dc techniques for the transport measurements and using heterodyne readout and demodulation techniques for the cQED measurements [19].

Having demonstrated the ability to probe the qubit JJ with both transport and cQED techniques, we next compare performance to a nominally identical gatemon without the FET and extra dc lead. Scanning electron micrographs of the two devices are shown in Figs. 2(a) and 2(b). The measured relaxation times  $T_1$  are shown for a range of qubit frequencies  $f_{01}$  controlled by  $V_Q$ , in Fig. 2(c). Relaxation times  $T_1$  were measured by applying a  $\pi$  pulse, calibrated by a Rabi experiment at  $f_{01}$ , followed by a variable wait time  $\tau$  before readout; see Fig. 2(c), inset.  $T_1(V_Q)$  were then extracted by fitting  $V_H(\tau)$  to a decaying exponential. We observe no systematic difference in  $T_1$  between the devices, demonstrating that the addition of a transport lead does not compromise the performance in the cQED configuration.

We next monitored  $dI_B/dV_B$ ,  $f_{01}$ , and  $T_1$  as  $V_{FET}$  was varied from off (cQED regime) to on (transport regime). Measurements of  $dI_B/dV_B$  [Fig. 3(a)] illustrate how the FET was turned conducting as  $V_{FET}$  was increased. Qubit frequency  $f_{01}$  was measured by two-tone spectroscopy, where a drive tone with varying frequency  $f_d$  was applied for 2  $\mu\text{s}$ , followed by a readout tone at  $f_R$ . A Lorentzian fit is used for each  $V_{FET}$  to extract  $f_{01}$ ; see Fig. 3(b), insets. We attribute the weak dependence of  $f_{01}$  on  $V_{FET}$  to cross talk between the two gates.

Following each spectroscopy measurement, a  $T_1$  measurement was immediately carried out, see Fig. 3(c), yielding a nearly gate independent  $T_1 \sim 6 \mu\text{s}$  for  $V_{FET} < -2$  V. At  $V_{FET} \sim -2$  V, we observe a sudden drop in  $T_1$ , followed by a short revival at  $V_{FET} \sim -1.8$  V. We associate the revival in  $T_1$  with the corresponding drop in  $dI_B/dV_B$  observed in

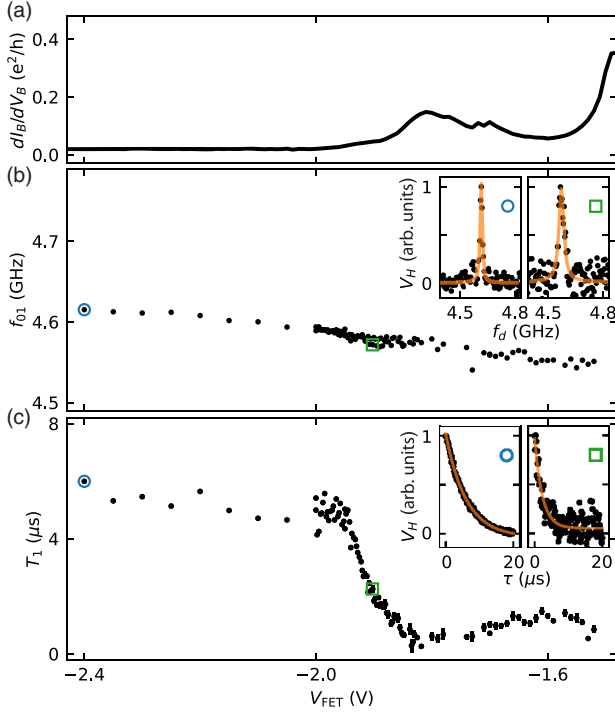


FIG. 3. (a) Differential conductance  $dI_B/dV_B$  as a function of FET gate voltage  $V_{FET}$  at high bias  $V_B = 1.0$  mV, to approximate normal-state resistance. (b) Qubit frequency  $f_{01}$  as a function of  $V_{FET}$  using two-tone spectroscopy. Insets: Lorentzian fits (orange) to data points in the main panel as indicated by the corresponding markers (blue circle, green square). From each  $V_H$  we subtract the background and normalize to the maximal value. (c) Similar to (b) relaxation times  $T_1$  from exponential fits (insets). Error bars are estimated from fit errors.

Fig. 3(a). We attribute this nonmonotonicity to the formation of quantum dots in the FET, which is commonly observed in nanowire JJs near the pinch-off values [20]. For  $V_{FET} > -1.5$  V,  $f_{01}$  and  $T_1$  can no longer be resolved, consistent with increasing  $dI_B/dV_B$ . We note that the  $dI_B/dV_B$  curve in Fig. 3(a) was shifted horizontally by a small amount (0.1 V) to align features in  $dI_B/dV_B$  with corresponding features in  $T_1$ . This was done to account for gate drift, as the cQED and transport measurements were performed sequentially over the course of several days.

We develop a circuit model of qubit relaxation in the leaded device. Within the model, the qubit circuit is coupled through the FET to a series resistance  $R_F$  and a parallel capacitance  $C_F$  representing an on-chip filter on the lead [21]. The coupling to the environment via the (superconducting) FET junction is modeled as a gate tunable Josephson inductance  $L_{FET}$ , giving a total environment impedance  $Z_{env} = i\omega L_{FET} + (1/R_F + i\omega C_F)^{-1}$ . This impedance can be viewed as a single dissipative element with resistance given by

$$R_{env} = 1/\text{Re}[Y_{env}] = L_{FET}^2 (R_F^2 C_F^2 \omega^4 + \omega^2) / R_F + R_F (1 - 2L_{FET} C_F \omega^2), \quad (1)$$

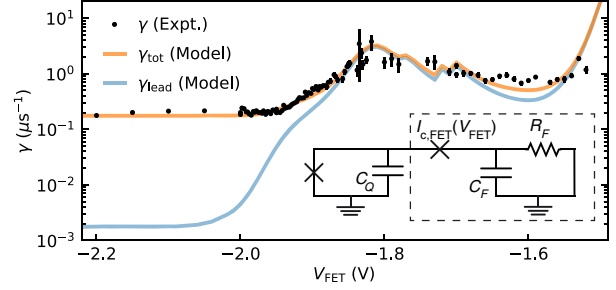


FIG. 4. Relaxation rate  $\gamma = 1/T_1$  (black circles) as a function of FET voltage  $V_{FET}$ , by inverting the experimental data from Fig. 3(c). Model relaxation rates  $\gamma_{lead}$  due only to the transport lead (blue) and  $\gamma_{tot}$  (orange) including lead and nonlead contributions (see text). The circuit model is sketched in the inset where the qubit is coupled to the environment by an effective impedance,  $Z_{env} = i\omega L_{FET} + (1/R_F + i\omega C_F)^{-1}$ . The dashed rectangle indicates the environment circuit.

with admittance  $Y_{env} = 1/Z_{env}$  [22]. The relaxation rate associated with the lead is given by  $\gamma_{lead} = 1/R_{env} C_Q$ , yielding a total decay rate  $\gamma_{tot} = \gamma_{nonleaded} + \gamma_{lead}$ , where  $\gamma_{nonleaded}$  is the decay rate associated with relaxation unrelated to the lead.

We estimate  $L_{FET} = \hbar/2eI_{c,FET}$  [23], where  $I_{c,FET}$  is the critical current of the FET, which we in turn relate to the normal-state resistance  $R_{n,FET}$  via the relation  $I_{c,FET} R_{n,FET} = \pi\Delta/2e$  [24], yielding

$$L_{FET} = \hbar R_{n,FET} / \pi\Delta. \quad (2)$$

$R_{n,FET}$  can be found from  $dI_B/dV_B$  in Fig. 3(a) by subtracting the voltage drop across the line resistance,  $R_{line} = 57$  k $\Omega$ , and assuming no voltage drop across the qubit JJ, justified by  $I_{c,FET} < I_c$ , where  $I_c$  is the critical current of the qubit JJ. From electrostatic simulations we estimate  $C_Q = 38$  fF [25]. We take  $\omega = 2\pi\overline{f_{01}}$ , where  $\overline{f_{01}} = 4.6$  GHz is the average  $f_{01}$  in Fig. 3(b), and  $\Delta = 190$   $\mu$ eV from Fig. 1(d). Combining Eqs. (1) and (2) with the measured  $1/T_1$  yields the  $\gamma_{lead}$  in Fig. 4 using  $R_F = R_{line}$  and  $C_F = 0.1$  pF as the best fit parameter. We note that electrostatic simulations give  $C_F \sim 0.5$  pF, in reasonable agreement with the best fit value. We define  $\gamma_{nonleaded} = 1/T_1^{\text{mean}}$ , where  $T_1^{\text{mean}} = 5.8$   $\mu$ s is the mean value of the  $T_1$  at  $V_{FET} < -2$  V. Using this estimate for  $\gamma_{nonleaded}$ , we calculate the total relaxation time based on the transport data (orange line in Fig. 4), showing excellent agreement with the measured values. The  $T_1$  limit based on the contribution of the lead saturates at  $T_1^{\text{lead}} \sim 1$  ms, indicating that leaded gatemon devices can accommodate large improvements in gatemon relaxation times. We mainly attribute the current level of relaxation times to dielectric losses. This is based on measurements of test resonators from the same substrates yielding quality factors of  $Q \sim 10^5$ , with  $T_1 \sim Q/(2\pi f_{01})$  being roughly consistent with the observed  $T_1$ . Although optimizing the qubit

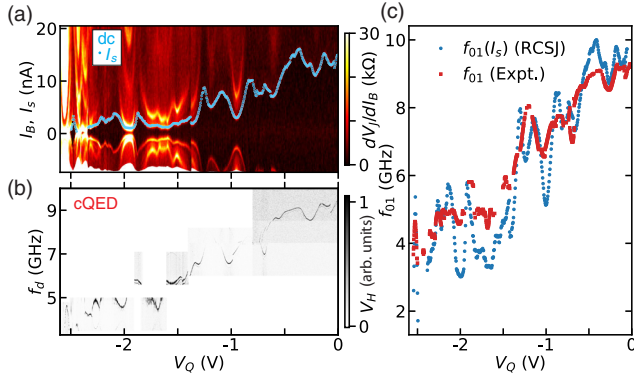


FIG. 5. (a) Differential resistance of the qubit JJ,  $dV_J/dI_B$ , as a function of current  $I_B$  and qubit gate voltage  $V_Q$ . Switching current  $I_s$  (blue points) from the edge of the zero-resistance state for increasing sweep at  $V_{\text{FET}} = +4$  V to turn the FET conducting. (b) Qubit frequency  $f_{01}$  from two-tone spectroscopy as a function of  $V_Q$ , acquired at  $V_{\text{FET}} = -3$  V to deplete the FET. The area of missing data at 5.0–5.6 GHz is due to  $f_{01}$  crossing the resonator frequency  $f_R$ . (c) Correlation between transport and cQED data.  $f_{01}$  from (b) (red) extracted as in Fig. 3(b), inset.  $f_{01}$  from  $I_c$  (blue) extracted by applying an RCSJ model to the data in (a) (see text).

lifetime is beyond the scope of this experiment, we are optimistic that these devices can reach similar coherence times as conventional superconducting qubits based on recent experiments of similar devices reaching  $T_1$  times of  $\sim 20 \mu\text{s}$  [26] and the promising upper limit on  $T_1$  of the model in Fig. 4.

Combining transport and cQED measurements allows for the correlation between critical current  $I_c(V_Q)$  and  $f_{01}(V_Q)$  to be observed directly [27]. The critical current  $I_c$  is extracted from  $dI_B/dV_B$  and  $I_B$  while sweeping  $V_B$  and  $V_Q$ . We extract the voltage drop and differential resistance across the qubit junction,  $V_J$  and  $dV_J/dI_B$ , by inverting  $dI_B/dV_B$  and subtracting  $R_{\text{line}}$ . In doing this, we assume that there is no voltage drop across the FET junction, since  $I_c < I_{c,\text{FET}}$ . The qubit resonance  $f_{01}$  is measured over the same  $V_Q$  range using two-tone spectroscopy; see Fig. 5(b). We note that the two-photon transition to the next harmonic is also observed for some  $V_Q$ , visible at a slightly lower frequency than  $f_{01}$ , given by the anharmonicity.

The relation between the two measurements is shown in Fig. 5(c). In order to estimate  $I_c(V_Q)$ , we first extract the switching current  $I_s(V_Q)$  from the data, taken as the  $I_B$  at which  $dV_J/dI_B$  is maximal, while sweeping  $I_B$  from negative to positive values [blue dots in Fig. 5(a)]. Bright features at high bias ( $I_B > I_s$ ) are likely associated with multiple Andreev reflection [28]. To extract  $I_c$  from the measured  $I_s$ , we model the qubit as an underdamped RCSJ (resistively and capacitively shunted junction) Josephson junction with a sinusoidal current-phase relation  $I = I_c \sin \phi$ . Furthermore, we note the small difference between the return current  $I_r$  (same definition as  $I_s$  at

negative  $I_B$ ) is slightly smaller than  $I_s$  [19]. In this case,  $I_s$  corresponds to the current of equal stability between the resistive and nonresistive state [29]. Under this condition, and for large quality factors  $Q \gg 1$ , the ratio  $I_s/I_c$  depends on quality factor  $Q = R\sqrt{2eI_cC_Q/\hbar}$  as

$$I_s/I_c = (2 + 4/\pi)Q^{-1} + (2 + \pi)Q^{-2}, \quad (3)$$

where  $R = (1/R_J + 1/R_{\text{line}})^{-1}$  and  $R_J$  is the shunt resistance [29]. In RCSJ theory  $R_J$  is proportional to the normal-state resistance of the junction  $R_N$  [9] with the proportionality depending on both the DOS inside the proximitized superconducting gap and temperature. As these parameters are not simultaneously accessible in our setup, we take the proportionality as a fit parameter. By doing so, we find  $R_J$  to be equal to  $R_N$ . We then apply the Ambegaokar-Baratoff relation  $I_c R_J = \pi\Delta/2e$  [24], which allows us to extract  $I_c$  by inverting Eq. (3) numerically [30]. The extracted  $I_c$ , in turn, yield values for  $Q$  in the range 10–20, consistent with our initial assumptions. For these values of  $Q$ , the RCSJ model takes the electron temperature to be  $>50$  mK to account for the weak asymmetry in  $I_s$  and  $I_r$  [19]. Finally, we relate  $I_c$  to  $f_{01}$  by using the numerical solution of the standard transmon Hamiltonian,  $H = 4E_C(n - n_g)^2 - E_J \cos(\phi)$  [31], with  $E_J = \hbar I_c/2e$  and  $E_C/h = e^2/2\hbar C_Q = 512$  MHz, at the charge degeneracy point with offset charge  $n_g = 0.5$ .

A comparison of the measured and estimated  $f_{01}$  is shown in Fig. 5(c). The model (RCSJ) curve is shifted horizontally by 0.05 V to align the features at  $\sim -2.5$  V and can be attributed to cross talk between the two gates as  $V_{\text{FET}}$  is varied from the dc to the cQED configuration, consistent with independent calibration measurements. A clear correlation is observed between the two measurement techniques, especially evident from the matching of local minima and maxima of both spectra and the overall agreement of the absolute values. We attribute the residual quantitative discrepancy to the simplifying assumptions used to determine the shunt resistance of the RCSJ model, which likely do not capture the possible gate dependence of the subgap DOS of the qubit JJ. In addition, the assumption of sinusoidal CPR will break down as the qubit JJ is opened due to increasing mode transmission in the semiconductor junction, leading to small overshoots of the model as perhaps seen around  $V_Q \sim 0$  V.

In summary, we have demonstrated the compatibility of dc transport and cQED measurement techniques in gate-mon qubits. This method may extend to other material platforms such as two-dimensional electron gases [15] or graphene [16,27,32]. Furthermore, we achieve a controllable relaxation rate potentially relevant for a range of qubit applications such as tunable coupling schemes [33,34] and controlled qubit relaxation and reset protocols [35,36]. In addition, we have demonstrated clear correlation between dc transport and cQED measurements motivating future

extensions, such as studying CPRs [8] or probing channel transmissions by studying multiple Andreev reflections [12] combined with cQED experiments [10,13,14]. Combining well-established transport techniques in quantum dot physics with qubit geometries may also be an interesting research direction [37]. Potentially, this geometry is also a promising platform to coherently probe Majorana zero modes in cQED measurements [38], as transport signatures have been demonstrated, both in half-shell nanowires [39] and full-shell wires [40,41].

This work was supported by Microsoft and the Danish National Research Foundation. We acknowledge Robert McNeil, Marina Hesselberg, Agnieszka Telecka, Sachin Yadav, Karolis Parfeniukas, Karthik Jambunathan, and Shivendra Upadhyay for the device fabrication. We thank Lucas Casparis and Roman Lutchyn for useful discussions, as well as Ruben Grigoryan for input on the electronic setup. B. v. H. thanks the Center for Quantum Devices, Niels Bohr Institute for the hospitality during part of the time in which this study was carried out.

- 
- [1] M. H. Devoret and R. J. Schoelkopf, *Science* **339**, 1169 (2013).
- [2] H. Paik, D. I. Schuster, L. S. Bishop, G. Kirchmair, G. Catelani, A. P. Sears, B. R. Johnson, M. J. Reagor, L. Frunzio, L. I. Glazman, S. M. Girvin, M. H. Devoret, and R. J. Schoelkopf, *Phys. Rev. Lett.* **107**, 240501 (2011).
- [3] L. Bretheau, Ç. Ö. Girit, H. Pothier, D. Esteve, and C. Urbina, *Nature (London)* **499**, 312 (2013).
- [4] Y.-J. Doh, J. A. van Dam, A. L. Roest, E. P. A. M. Bakkers, L. P. Kouwenhoven, and S. De Franceschi, *Science* **309**, 272 (2005).
- [5] T. W. Larsen, K. D. Petersson, F. Kuemmeth, T. S. Jespersen, P. Krogstrup, J. Nygård, and C. M. Marcus, *Phys. Rev. Lett.* **115**, 127001 (2015).
- [6] G. de Lange, B. van Heck, A. Bruno, D. J. van Woerkom, A. Geresdi, S. R. Plissard, E. P. A. M. Bakkers, A. R. Akhmerov, and L. DiCarlo, *Phys. Rev. Lett.* **115**, 127002 (2015).
- [7] A. A. Golubov, M. Y. Kupriyanov, and E. Il'ichev, *Rev. Mod. Phys.* **76**, 411 (2004).
- [8] E. M. Spanton, M. T. Deng, S. Vaitiekėnas, P. Krogstrup, J. Nygård, C. M. Marcus, and K. A. Moler, *Nat. Phys.* **13**, 1177 (2017).
- [9] M. Tinkham, *Introduction to Superconductivity* (Courier Corporation, New York, 2004).
- [10] L. Tosi, C. Metzger, M. F. Goffman, C. Urbina, H. Pothier, S. Park, A. L. Yeyati, J. Nygård, and P. Krogstrup, *Phys. Rev. X* **9**, 011010 (2019).
- [11] K. Zuo, V. Mourik, D. B. Szombati, B. Nijholt, D. J. van Woerkom, A. Geresdi, J. Chen, V. P. Ostroukh, A. R. Akhmerov, S. R. Plissard, D. Car, E. P. A. M. Bakkers, D. I. Pikulin, L. P. Kouwenhoven, and S. M. Frolov, *Phys. Rev. Lett.* **119**, 187704 (2017).
- [12] M. F. Goffman, C. Urbina, H. Pothier, J. Nygård, C. M. Marcus, and P. Krogstrup, *New J. Phys.* **19**, 092002 (2017).
- [13] A. Kringhøj, L. Casparis, M. Hell, T. W. Larsen, F. Kuemmeth, M. Leijnse, K. Flensberg, P. Krogstrup, J. Nygård, K. D. Petersson, and C. M. Marcus, *Phys. Rev. B* **97**, 060508(R) (2018).
- [14] M. Hays, G. de Lange, K. Serniak, D. J. van Woerkom, D. Bouman, P. Krogstrup, J. Nygård, A. Geresdi, and M. H. Devoret, *Phys. Rev. Lett.* **121**, 047001 (2018).
- [15] L. Casparis, M. R. Connolly, M. Kjaergaard, N. J. Pearson, A. Kringhøj, T. W. Larsen, F. Kuemmeth, T. Wang, C. Thomas, S. Gronin, G. C. Gardner, M. J. Manfra, C. M. Marcus, and K. D. Petersson, *Nat. Nanotechnol.* **13**, 915 (2018).
- [16] J. I.-J. Wang, D. Rodan-Legrain, L. Bretheau, D. L. Campbell, B. Kannan, D. Kim, M. Kjaergaard, P. Krantz, G. O. Samach *et al.*, *Nat. Nanotechnol.* **14**, 120 (2019).
- [17] J. J. Riquelme, L. de la Vega, A. L. Yeyati, N. Agrat, A. Martin-Rodero, and G. Rubio-Bollinger, *Europhys. Lett.* **70**, 663 (2005).
- [18] P. Krogstrup, N. L. B. Ziino, W. Chang, S. M. Albrecht, M. H. Madsen, E. Johnson, J. Nygård, C. M. Marcus, and T. S. Jespersen, *Nat. Mater.* **14**, 400 (2015).
- [19] See Supplemental Material at <http://link.aps.org/supplemental/10.1103/PhysRevLett.124.056801> for additional details on the experimental setup and on the critical current analysis.
- [20] W. Chang, S. M. Albrecht, T. S. Jespersen, F. Kuemmeth, P. Krogstrup, J. Nygård, and C. M. Marcus, *Nat. Nanotechnol.* **10**, 232 (2015).
- [21] X. Mi, J. Cady, D. Zajac, J. Stehlik, L. Edge, and J. R. Petta, *Appl. Phys. Lett.* **110**, 043502 (2017).
- [22] A. A. Houck, J. A. Schreier, B. R. Johnson, J. M. Chow, J. Koch, J. M. Gambetta, D. I. Schuster, L. Frunzio, M. H. Devoret, S. M. Girvin, and R. J. Schoelkopf, *Phys. Rev. Lett.* **101**, 080502 (2008).
- [23] S. M. Girvin, in *Quantum Machines: Measurement and Control of Engineered Quantum Systems*, Lecture Notes of the Les Houches Summer School, Vol. 96 (Oxford University Press, Oxford, 2014).
- [24] V. Ambegaokar and A. Baratoff, *Phys. Rev. Lett.* **11**, 104 (1963).
- [25] COMSOL, Inc., [www.comsol.com](http://www.comsol.com).
- [26] F. Luthi, T. Stavenga, O. W. Enzing, A. Bruno, C. Dickel, N. K. Langford, M. A. Rol, T. S. Jespersen, J. Nygård, P. Krogstrup, and L. DiCarlo, *Phys. Rev. Lett.* **120**, 100502 (2018).
- [27] F. E. Schmidt, M. D. Jenkins, K. Watanabe, T. Taniguchi, and G. A. Steele, *Nat. Commun.* **9**, 4069 (2018).
- [28] T. Klapwijk, G. Blonder, and M. Tinkham, *Physica (Amsterdam)* **109(B+C)**, 1657 (1982).
- [29] R. L. Kautz and J. M. Martinis, *Phys. Rev. B* **42**, 9903 (1990).
- [30] Numerical code and data accompanying the analysis of Fig. 5(c) are found at [https://github.com/anderskringhoej/dc\\_qubit](https://github.com/anderskringhoej/dc_qubit).
- [31] J. Koch, T. M. Yu, J. M. Gambetta, A. A. Houck, D. I. Schuster, J. Majer, A. Blais, M. H. Devoret, S. M. Girvin, and R. J. Schoelkopf, *Phys. Rev. A* **76**, 042319 (2007).
- [32] J. Kroll, W. Uilhoorn, K. van der Enden, D. de Jong, K. Watanabe, T. Taniguchi, S. Goswami, M. Cassidy, and L. Kouwenhoven, *Nat. Commun.* **9**, 4615 (2018).
- [33] Y. Chen *et al.*, *Phys. Rev. Lett.* **113**, 220502 (2014).

- [34] L. Casparis, N. J. Pearson, A. Kringhøj, T. W. Larsen, F. Kuemmeth, J. Nygård, P. Krogstrup, K. D. Petersson, and C. M. Marcus, *Phys. Rev. B* **99**, 085434 (2019).
- [35] P. J. Jones, J. A. M. Huhtamäki, J. Salmilehto, K. Y. Tan, and M. Möttönen, *Sci. Rep.* **3**, 1987 (2013).
- [36] R. Ma, B. Saxberg, C. Owens, N. Leung, Y. Lu, J. Simon, and D. I. Schuster, *Nature (London)* **566**, 51 (2019).
- [37] S. De Franceschi, L. Kouwenhoven, C. Schönenberger, and W. Wernsdorfer, *Nat. Nanotechnol.* **5**, 703 (2010).
- [38] E. Ginossar and E. Grosfeld, *Nat. Commun.* **5**, 4772 (2014).
- [39] V. Mourik, K. Zuo, S. M. Frolov, S. R. Plissard, E. P. A. M. Bakkers, and L. P. Kouwenhoven, *Science* **336**, 1003 (2012).
- [40] R. M. Lutchyn, G. W. Winkler, B. Van Heck, T. Karzig, K. Flensberg, L. I. Glazman, and C. Nayak, *arXiv:1809.05512*.
- [41] S. Vaitiekėnas, M.-T. Deng, P. Krogstrup, and C. M. Marcus, *arXiv:1809.05513*.